Bioinspiration &
Biomimetics

PAPER • OPEN ACCESS

Development of a turning control strategy for a bio-inspired underwater vehicle

To cite this article: Owen McKenney *et al* 2025 *Bioinspir. Biomim.* **20** 056004

IOP Publishing Bioinspir. Biomim. 20 (2025) 056004 https://doi.org/10.1088/1748-3190/adf67a

Bioinspiration & Biomimetics

OPEN ACCESS

RECEIVED
1 May 2025

REVISED
8 July 2025

ACCEPTED FOR PUBLICATION
31 July 2025

PUBLISHED
19 August 2025

PAPER

Development of a turning control strategy for a bio-inspired underwater vehicle

Owen McKenney, Joseph Zhu, Tianjun Han and Hilary Bart-Smith*

Department of Mechanical and Aerospace Engineering, University of Virginia, Charlottesville, VA, United States of America

* Author to whom any correspondence should be addressed.

E-mail: hb8h@virginia.edu

Keywords: bio-inspired propulsion, underwater vehicle, turning, control

Abstract

Maneuvering in fish is complex and offers inspiration in the development of the next generation bio-inspired underwater vehicles (BUVs). Balancing desired functionality with minimal mechanical complexity is a challenge in developing a BUV. This study presents a single-actuator turning strategy for the Tunabot, a bio-inspired robotic fish, using asymmetric tail-beat timing to generate turning forces. Biological fish, such as tuna, adjust tail kinematics for maneuverability. Following this principle, the proposed control method modifies stroke duration through a single motor, synchronized by a digital encoder. Experiments were conducted in a tank, using the dorsal-view high-speed video and DeepLabCut motion tracking technology to analyze and quantify turning radius and swimming velocity. A 66% asymmetric difference in tail-beat timing resulted in a turning radius of 1.42 body lengths at a certain base frequency. Scaling laws were developed to reveal the fluid dynamics and predict the turning radius and swimming speed of the Tunabot given known tailbeat frequencies. Power consumption data was gathered for asymmetric maneuvers and compared to their symmetric equivalents. These findings demonstrate that asymmetric tail-beat control enables effective turning without dedicated steering mechanisms, offering novel insights for designing highly maneuverable underwater bio-robots with low power consumption.

1. Introduction

Various fish species are being extensively studied for their high-speed and high-efficient swimming capabilities, to enable energy-efficient locomotion at sustained velocities in bio-inspired underwater vehicles (BUVs) [1, 2]. However, these platforms often lack the necessary maneuverability, a critical limitation for real-world applications in dynamic environments where rapid directional adjustments are essential. Most existing designs depend on single-motor propulsion systems that drive rigid or semi-rigid tails at high frequencies, prioritizing thrust over agility. While these systems excel in linear speed and simplicity, their inability to execute turning maneuvers restricts their practical applicability.

Existing approaches to enhance maneuverability often involve trade-offs. For example, articulated tails with multiple servo-driven joints [3–5] or external actuators such as pectoral fins [6–8] enable turning but introduce increased power consumption, mechanical complexity, and additional weight. These modifications place greater demands on onboard power systems, thereby reducing operational endurance, an especially critical limitation for compact, battery-constrained platforms.

To address this limitation, this study integrates turning capabilities with a single motor thunniform swimmer, the Tunabot [1], without the addition of auxiliary actuators or significant mechanical redesign. By leveraging the existing propulsion system, we achieve directional control while retaining its proven high-speed performance. This strategy eliminates power overhead and avoids space, weight, and complexity penalties inherent to multi-actuator systems.

Focusing on biological systems, thunniform swimmers have several adaptations to execute turning maneuvers, such as pectoral fins and caudal fin manipulation. Recent studies on the Pacific bluefin tuna suggest that these kinds of thunniform swimmers have three main behaviors for turning [9]. Classified as glide turns, powered turns, and ratchet turns, these maneuvers offer trade-offs between energy expenditure, turning rate, and turning radius.

This study focuses on implementing a caudal-based turning method that leverages an asymmetric frequency difference across a single tailbeat to achieve turning. Similar turning behavior was observed by Downs *et al* [9], who reported that Pacific bluefin tuna varied their tailbeats asymmetrically to achieve both large and small radius turning. Downs *et al* categorizes these active tailbeat asymmetric maneuvers into two different categories: powered turning and ratchet turning. Powered turning relies on small asymmetric differences, leading to wide radius maneuvers, while ratchet turning relies on larger asymmetric differences, resulting in smaller radius maneuvers [9]. The ability to control this asymmetric difference in the tailbeat allows the tuna to have a large degree of flexibility in its heading, leading to increasingly accurate navigation.

In a bio-inspired swimmer such as the Tunabot, the ability to adapt its turning radius through an asymmetric flapping turning strategy enables the vehicle to execute a wide range of turning radii while still maintaining sufficient propulsive forces. This study attempts to recreate this turning behavior using an existing tuna-inspired swimming platform with an asymmetric tailbeat pattern to emulate the turning behavior of an equivalent biological thunniform swimmer.

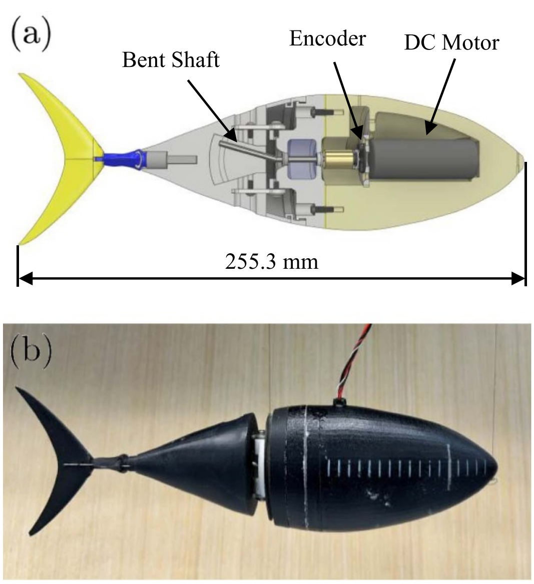

Figure 1. (a) Dorsal–ventral cross section view of the Tunabot CAD model, (b) dorsal–ventral view of Tunabot.

2. Design & control methods

This study adapts an existing thunniform swimming platform, the Tunabot [1], with targeted mechanical modifications to enable turning capabilities. Various caudal fin flapping configurations were explored, and a control strategy was developed to successfully regulate the tailbeat frequency of the vehicle.

2.1. Mechanical design

The original Tunabot design was optimized for high-speed rectilinear swimming, featuring a 3D-printed ABS body with a single articulated point driving the caudal fin. The Tunabot measures 255.3 mm in length, 49.2 mm in width, and 67.8 mm in height. It has a mass of 0.31 kg in the air. As seen in figures 1(a) and (b), the vehicle consists of three main sections: the head, actuating region, and caudal fin.

With the objective of this study being to add a new degree of maneuverability to an existing vehicle, a number of design changes were made to the vehicle model. The caudal fin is driven by a DC Motor (485 RPM Econ Gear Motor; gear ratio 20:1) from ServoCity, differing from the original Tunabot design which utilized a 970 RPM motor, limiting the study to a lower frequency range. Pulse-width modulation (PWM) signals were sent to the motor to control speed from an external control board. The caudal fin is actuated through a mechanical linkage between the motor shaft and the inside of the tail. This linkage creates a proportional relationship between motor speed and tailbeat frequency, allowing for the frequency of the tail to be manipulated by motor control. The vehicle was powered via an external 12 V power supply and was electrically tethered by a cable with a diameter of approximately 2.5 mm.

A digital encoder (US Digital E16 16 mm Micro Optical Encoder; 2048 cycles per revolution) was used to accurately obtain positional data from the propulsion motor. This encoder provides A, B, and Index digital quadrature signals with a small physical footprint, making it an optimal choice for usage inside the space-constrained Tunabot model. The bore size of the optical encoder disk, initially 2 mm, was carefully modified to fit around the 4 mm shaft of the propulsion motor. A small 3D-printed disk-to-shaft adapter was printed to ensure a rigid yet easily modifiable coupling between the disk and the motor shaft. The digital outputs from the A and B channels of the encoder were monitored via digital interrupts to track the motor's position in encoder ticks about its cycle. Additionally, the output from the index channel was monitored to log the completion of the motor's cycle. The encoder disk was mounted such that the position of the index corresponded with a colinear tail position with respect to the propulsion axis of the Tunabot. A homing sequence was written to initialize the tail to a consistent position for each test.

2.2. Caudal fin flapping configurations

This work focused on the implementation of an asymmetric flapping turning strategy. The principle underlying this approach is the modulation of the caudal fin's tailbeat frequency during specific phases of the propulsion cycle, thereby generating a frequency bias across the sweeping path of the fin. This movement results in a turning maneuver towards the side of the tailbeat of lower frequency. It is important to note that this method only creates a frequency bias and does not introduce any positional bias of the tailbeat.

During our preliminary investigations, a positional bias turning method was considered. In this half cycle flapping approach, turning is achieved by introducing a positional tailbeat bias, angling the sweeping path towards a single direction to generate a lateral turning force. Qualitative comparisons between the two methods indicate that half cycle flapping generates less propulsive force as the tail no longer follows its full path. In contrast, asymmetric flapping produces a greater propulsive force as the tail is still following its full path. In addition, in-water testing of the half cycle flapping method revealed major vehicle instability issues about the propulsion axis of the Tunabot due to the fast switching of motor direction necessary to create the positional bias. As a result, this strategy was not pursued further, and no control method was developed.

Implementing an asymmetric approach requires identifying an optimal division of the motor's cycle to achieve effective turning. Open-loop control was developed for four different configurations of asymmetric flapping, each manipulating the frequency of the motor at different points during its cycle. Through qualitative testing in a free-swimming setup and analysis of live encoder data, it was determined that dividing the motor's cycle into two equal sections provided the most pronouncing heading change and the best qualitive swimming performance. Specifically, the cycle was partitioned from 0° to 180° and from 180° to 360°, with 0° defined at the top of the cycle. This division resulted in a tailbeat frequency f_1 on the left half of the sweeping path and a tailbeat frequency f_2 on the right half, successfully creating a frequency bias that enabled effective turning maneuvers.

2.3. Control strategy

To regulate the frequency of the propulsion motor, a proportion-derivative (PD) controller was implemented. PD control is a widely used feedback control strategy that adjusts the motor output based on the error between a desired setpoint and the measured system response. Integral control was excluded due to the rapid change in setpoint. Figure 2 provides a simple outline of the control strategy used. For this system, the desired setpoint was a frequency value

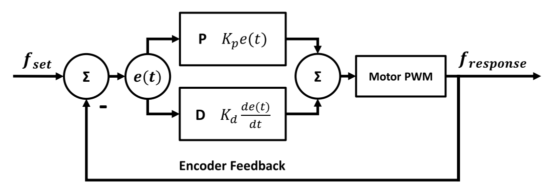

Figure 2. PD control scheme diagram.

ranging from 1 to 5 Hz, with the measured output being the actual motor frequency. This control strategy was used to adjust the PWM signal, ensuring a fast response to the changing input frequency. PWM signals were clamped from 70 to 255, with 70 being the lowest possible PWM signal that would actuate the motor. For quick response in the system output, step functions were used to oscillate between the two asymmetric flapping frequencies.

Real-time encoder feedback was used to calculate the motor's instantaneous frequency. The calculation was based on comparing the current encoder sample E_1 with the previous encoder sample E_2. Using this difference, along with the encoder's counts per revolution, denoted as n, and a known time interval $\mathrm{d}t$, the actual frequency of the tailbeat f_i could be acquired at any given location on the motor's cycle using

$$f_i = \frac{E_1 - E_2}{\mathrm{d}t \cdot n}. \tag{1}$$

To minimize noise within frequency calculations, a first-order low-pass filter was applied using an exponential moving average to calculate filtered frequency f_f using

$$f_\mathrm{f} = \alpha f_i + (1-\alpha) f_{\mathrm{f,\,prev}}. \tag{2}$$

This filter smooths fluctuations in encoder readout by blending the current encoder measurement with the previously filtered value $f_{\mathrm{f,\,prev}}$. By adjusting the filter weight α, noise could be sufficiently attenuated, enabling the PD controller to be less susceptible to error and fluctuation in frequency calculations. Using these control strategies, the speed of the motor was modulated, enabling controllable asymmetric flapping. Real-time encoder data shown in figure 3(a) indicates that noticeable oscillations persisted in the motor output frequency. We attribute the observed oscillations to the mechanical linkage between the motor and the caudal fin, which likely introduces variable friction points throughout the motor cycle. These friction variations perturb the PD controller as it attempts to maintain a constant frequency under changing resistance. The accuracy of the frequency response depended on both the magnitude of the difference between the two selected

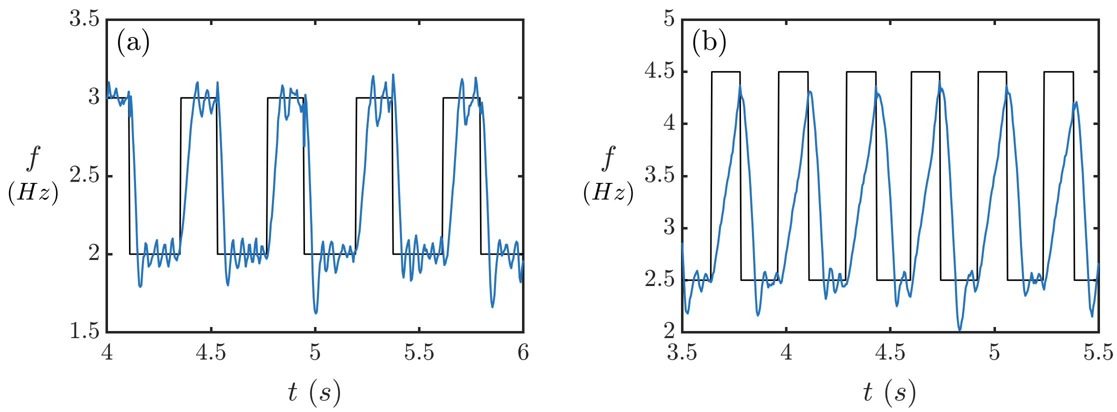

Figure 3. Instantaneous motor frequency gathered from encoder readings. Blue line represents calculated frequency with black line representing set frequency. (a) Asymmetric routine between 2 and 3 Hz, (b) asymmetric routine between 4.5 and 2.5 Hz.

frequencies and the base frequency value used for the asymmetric flapping protocol. Larger frequency differences resulted in poorer system performance, whereas lower base frequencies combined with smaller frequency differences produced more consistent and accurate responses, as shown in figure 3. Constraints in the motor's ability to adapt to rapid PWM changes likely contributed to the difficulty in achieving stable frequency tracking for larger frequency differences. Nevertheless, this control strategy provided a reliable method for regulating the propulsion motor between two distinct frequencies, producing enough disparity between frequencies to generate an observable and quantifiable asymmetric turning maneuver.

An important consideration of this asymmetric control strategy is the potential time delay in the start of a turning maneuver. Based on the sectioning of the motor cycle, the asymmetric routine can only be initiated at two points during the motor's cycle, either when the motor is at 0° or 180°. This time delay will occur when transitioning from symmetric to asymmetric flapping and will be particularly noticeable at lower frequencies. Time delay will be worst when the asymmetric control is initiated at an undesirable motor position such as 1° or 181°. The relationship between time delay t_d and the symmetric flapping frequency f_s is governed by

$$t_\mathrm{d} = \frac{0.5}{f_\mathrm{s}}. \tag{3}$$

The relationship between t_d and f_s is inversely proportional, and at frequencies greater than 5 Hz, this delay becomes increasingly negligible.

3. Experimental methods

To evaluate the performance of the asymmetric flapping control algorithm, a range of frequency combinations was tested using base frequencies between 2.5 and 5 Hz in 0.5 Hz increments. Each base frequency f_1 was combined with a frequency difference Δf defined by equations (4) and (5). Equation (6) represents the resultant secondary frequency f_2, the difference of f_1 and Δf,

$$f_1 \in \{2.5, 3, 3.5, 4, 4.5, 5\} \tag{4}$$

$$\Delta f \in \{0.5, 1, 1.5, 2\} \tag{5}$$

$$f_2 = f_1 - \Delta f. \tag{6}$$

Frequency combinations with disparities greater than 2 Hz were generally ineffective due to limitations in the motor's response time, leading to a loss of control. Likewise, at base frequencies above 5 Hz, the motor exhibited difficulty transitioning to f_2, also resulting in control loss. Therefore, only a range of base frequency f_1 from 2.5 to 5 Hz was considered. Frequency combinations having a base frequency lower than 2.5 Hz resulted in impractically low swimming speeds. Additionally, frequency values f_2 lower than 1 Hz were not considered for the same reason, meaning the combination $f_1 = 2.5, \Delta f = 2.0$ was excluded from testing. Each frequency combination was tested over 3 trials, resulting in a total of 69 datapoints.

3.1. Experimental setup

Frequency combinations were tested in an open water tank measuring 4.8 m × 1.5 m. Although experiments aimed to simulate free-swimming conditions, the Tunabot model remained electrically tethered to supply continuous power and eliminate the need for post-experiment data retrieval. To minimize the influence of the tether, the Tunabot platform was adjusted to be neutrally buoyant, and the electrical cable was suspended along the vehicle's y-axis with sufficient slack to avoid mechanical interference. Under these conditions, tether effects were considered

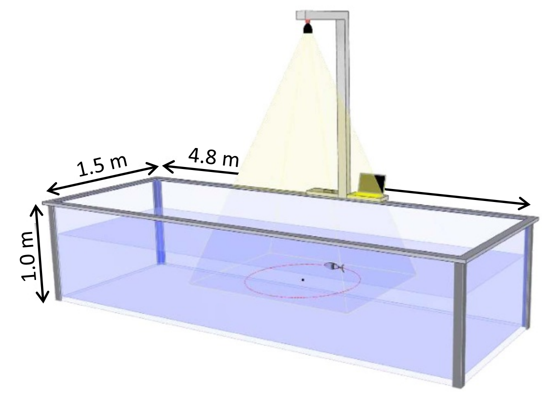

Figure 4. Schematic diagram of the experimental setup.

negligible and excluded from analysis. All tests were conducted with the Tunabot submerged at the mid-depth of the tank to minimize interference from the surface and bottom boundaries. During each trial, the Tunabot operated at the assigned frequency combination until it exited the camera frame, made contact with a tank wall, or completed a full rotational turn. Dorsal-view high-speed video was recorded at 100 fps for each test using an AOS Technologies PROMON U1000 streaming camera mounted above the tank to capture the full testing area. Figure 4 depicts the full testing setup used for experimentation.

3.2. Data analysis techniques

High-speed video recordings were analyzed using DeepLabCut (DLC), an open-source software package for markerless pose estimation that utilizes transfer learning with deep neural networks [10]. The video data was manually labeled, and a network was trained to extract the Tunabot's pose as a series of $x-y$ coordinates for each trial. To enhance the robustness of pose estimation, two points aligned along the Tunabot's body axis were tracked, providing two sets of $x-y$ coordinates per test. Network evaluation yielded an average tracking confidence of 97.88% across all trials. Minor disturbances in pose estimation occasionally occurred due to glare on the water's surface and visual interference from cables, which sometimes obscured the tracking markers. Figure 5 shows DLC-labeled snapshots of an experimental test at different time values, showing that DLC training is robust enough to successfully track the Tunabot even with disturbances.

After extracting the coordinate data, a scalar conversion factor m (in mm/pixel) was applied to transform pixel-based values into millimeters. This factor was determined using a calibration video with a known distance and was recorded at the same height as the Tunabot during turning experiments. This constant was found to be $p = 1.097025$ mm/pixel. Subsequently, the coordinate data from each trial was imported into MATLAB for analysis. A least-squares circle fitting method was employed to estimate the turning radius of the vehicle. The total turn angle θ and turn duration Δt were calculated using the start and end coordinates along with their respective timestamps. The angular velocity of the turning maneuver was computed using the definition provided in equation (7). The corresponding linear velocity V during the turn was derived using the turning radius r and angular velocity ω using the tangential linear velocity relation in equation (8),

$$\omega = \frac{\theta}{\Delta t} \tag{7}$$

$$V = r\omega. \tag{8}$$

Power consumption P was measured and averaged for each frequency combination using an INA260 sensor. Measurements were not taken until the Tunabot had reached steady state and were collected for at least 20 flapping cycles. This power P is the summation of the power consumed by the motor and the motor driver.

4. Experimentation results

Following data extraction from the DLC-generated CSV files, analysis was conducted in MATLAB. Figure 6(a) presents raw data points, with radius r plotted against velocity V. Figures 6(c) and (d) present various trajectories of the Tunabot. As shown in figure 6(a), larger frequency differences Δf combined with lower base frequencies f_1 generally resulted in a smaller turning radius and lower velocity. In contrast, smaller Δf and larger f_1 values tend to result in maneuvers with a larger turning radius and larger velocity. From the plot in 6(a), turning rates can be calculated for each data point by solving for ω in equation (8). Greater Δf values correspond to faster turning rates, whereas smaller Δf are associated with slower turning rates. Data points featuring both high base frequencies and large frequency differences yield the fastest turning rates. These results collectively indicate that both the magnitude of the base frequency and the extent of the frequency disparity play critical roles in determining maneuvering performance.

Analysis of the raw turning paths extracted from the DLC tracking highlights the significant influence of f_1 and Δf on the resulting turning radius. Figure 6(c) presents representative turning paths for each f_1 value at a fixed $\Delta f = 2.0$. Consistent with the trends observed in figure 6(a), smaller f_1 values produced tighter turning paths. Conversely, figure 6(d) displays turning paths at various f_1 values with a smaller fixed $\Delta f = 0.5$ Hz, resulting in a noticeably larger

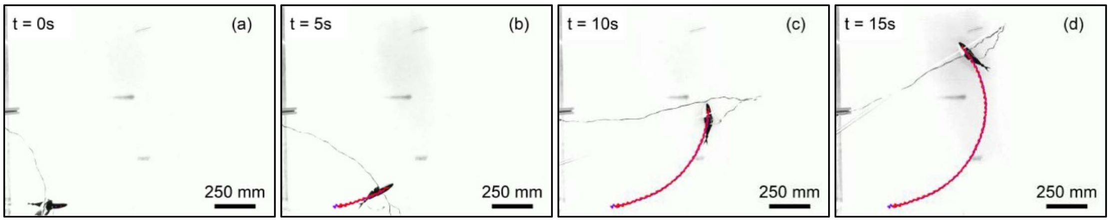

Figure 5. Pictures taken from Tunabot turning testing at $f_1 = 4.5$ Hz, $\Delta f = 2.0$ Hz. (a) Position at $t = 0$, (b) $t = 5$, (c) $t = 10$, (d) $t = 15$. Motion traces have been added to the images with the red trace tracking a point on the Tunabot's head, and the purple tracking a point 24.2 mm behind this first point.

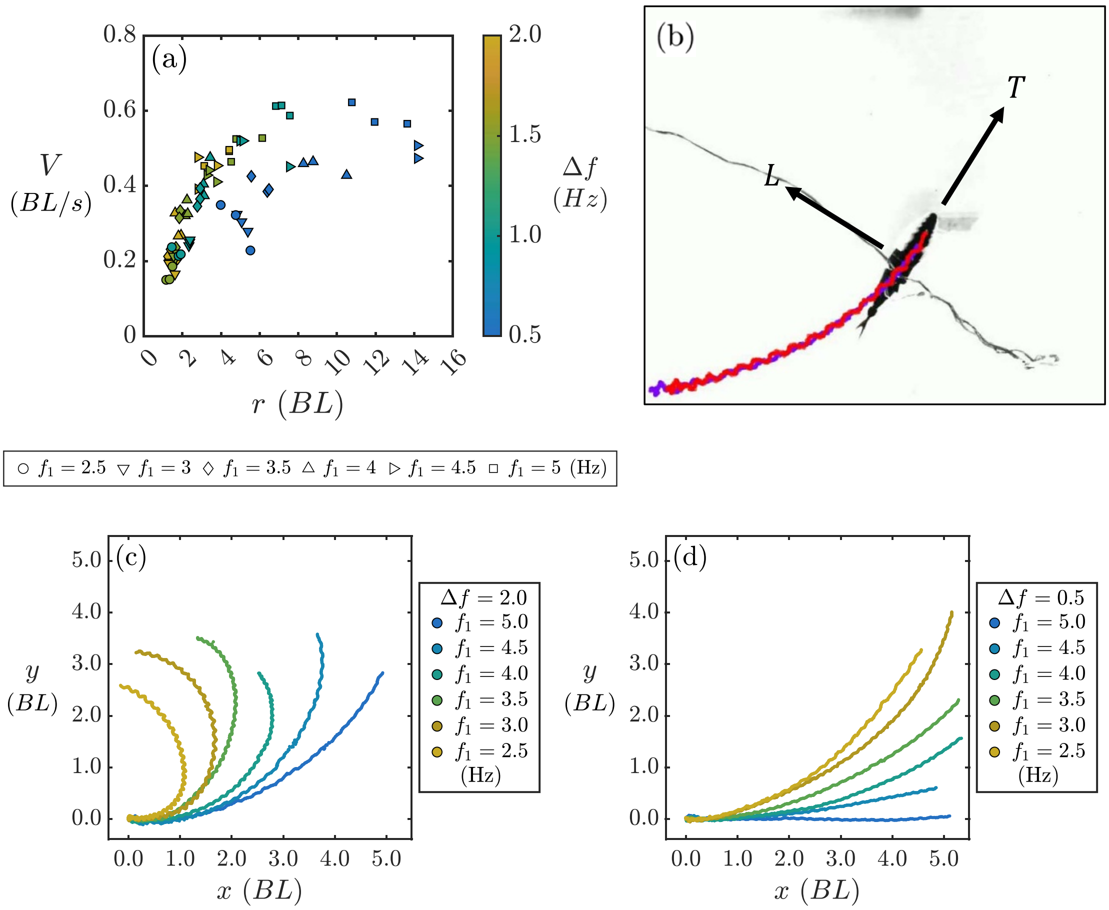

Figure 6. (a) Velocity and turning radius measured at different frequency combinations. The marker styles are mapped to the value of f_1 while the marker colors, from blue to yellow, correspond to Δf from 0.5 to 2 Hz. (b) Lift and thrust forces acting on the Tunabot. Trajectories of the Tunabot at different values of f_1 when Δf is fixed at (c) 2 Hz and (d) 0.5 Hz.

turning radius. These results further demonstrate the combined effects of base frequency and frequency disparity on maneuvering performance.

Building on this analysis of turning trajectories, we assessed the range and adaptability of turning radii achieved through the tested frequency combinations. Varying the input frequencies produced a broad spectrum of turning behaviors, with radii spanning from 1.33 to 14.90 body lengths (BL), representing the minimum and maximum values observed i experimentation. Figures 6(c) and (d) illustrate the large range of turning radius flexibility achieved with this approach. This range can be resolved even more finely when using frequency combinations without the 0.5 Hz step size constraint and limiting the maximum Δf to 2.0 Hz. For bio-inspired underwater vehicles, such control flexibility is essential, as the optimal turning radius is often dictated by environmental or operational requirements. A larger turning radius, which produces a gradual change in heading while maintaining forward velocity, may be better suited for long-distance navigation. In contrast, a smaller turning radius with faster heading changes could be advantageous in dense schooling contexts or during short-range obstacle avoidance.

Interestingly, frequency combinations of different f_1 and Δf can produce similar turning radius while yielding substantial differences in swimming velocity. For instance, trials using $f_1 = 5$ Hz, $\Delta f = 2$ Hz resulted in an average turning radius and speed of 3.99 BL and 0.59 BL s^{-1}, respectively. Trials with $f_1 = 2.5$ Hz, $\Delta f = 0.5$ Hz produced an average turning radius 4.75 BL and a swimming speed of 0.30 BL s^{-1}. Comparing these two combinations, the $f_1 = 5$ Hz case exhibited a 19.05% decrease in turning radius and a corresponding 44.21% increase in swimming speed relative to the $f_1 = 2.5$ Hz case. These results suggest that turning maneuvers of comparable radius can be achieved at different swimming speeds, offering an additional degree of control that may be advantageous depending on specific maneuvering requirements.

5. Scaling law analysis

Scaling laws were developed to reveal the physics of the asymmetric flapping of the Tunabot and to predict its velocity and turning radius. Here, we approximate the propulsor of the Tunabot, which is the actuation section plus the tail, as an airfoil pitching about its leading edge. The reduced frequency, $k = fc/V$, of the propulsor in the experiments ranges from 1.33 to 1.51, where f is the flapping frequency and c is the chord length of the propulsor. Based on linear aerodynamic theory [11–14], the added mass force, which results from the acceleration of the surrounding fluid by the propulsor, dominates the force acting on the propulsor in the reduced frequency range of this study. Therefore, we only account for the added mass force in the scaling law development. According to linear aerodynamic theory, the time-averaged lift L, which is effectively the centripetal force in our experiments as depicted in figure 6(b), can be calculated as

$$L \propto \rho S A c f_1^2 \left(\frac{\frac{1}{f_1}}{\frac{1}{f_1} + \frac{1}{f_1 - \Delta f}} \right) - \rho S A c (f_1 - \Delta f)^2 \left(\frac{\frac{1}{f_1 - \Delta f}}{\frac{1}{f_1} + \frac{1}{f_1 - \Delta f}} \right), \tag{9}$$

where ρ is the density of the fluid, S is the planform area of the propulsor, and A is the tailbeat amplitude. After organization, we are left with

$$L \propto \rho S A c \left(\frac{f_1^2 (f_1 - \Delta f) - (f_1 - \Delta f)^2 f_1}{2 f_1 - \Delta f} \right). \tag{10}$$

When the frequency asymmetry is set to $\Delta f = 0$, equation (10) becomes $L = 0$, indicating that no centripetal force is generated. Similarly, the time-averaged thrust T acting on the Tunabot as depicted in figure 6(b) can be calculated as

$$T \propto \rho S A^2 \left(\frac{f_1^2 (f_1 - \Delta f) + (f_1 - \Delta f)^2 f_1}{2 f_1 - \Delta f} \right). \tag{11}$$

When the frequency asymmetry is equal to $\Delta f = 0$, equation (11) is reduced to

$$T \propto \rho S A^2 f_1^2, \tag{12}$$

which is exactly the added mass thrust scaling of an airfoil symmetrically pitched about its leading edge. According to the drag law of biological swimming [15, 16] the thrust generated by the propulsor is equal to the drag produced by the fish head when the Tunabot reaches the steady state, which is

$$T = D = 0.5 \rho V^2 L_i S, \tag{13}$$

where L_i is the Lighthill number that indicates the level of drag loading on the fish head. The Lighthill number is related to the material and geometry of the Tunabot, which was fixed in our experiments. Combining equations (11) and (13), the velocity can be calculated as

$$V \propto \sqrt{\frac{A^2}{Li} \left(\frac{f_1^2 (f_1 - \Delta f) + (f_1 - \Delta f)^2 f_1}{2 f_1 - \Delta f} \right)}. \tag{14}$$

Since the amplitude and the Lighthill number in our experiments were fixed, we can wrap them into a constant, resulting in

$$V = c_1 \sqrt{\frac{f_1^2 (f_1 - \Delta f) + (f_1 - \Delta f)^2 f_1}{2 f_1 - \Delta f}}, \tag{15}$$

where c_1 is a dimensional constant and needs to be determined. The coefficient is determined to be $c_1 = 0.12$ by linear regression. Figure 7(a) compares the scaling law prediction with experimental data, which shows that the model can predict the velocity of the Tunabot to within 20% error. According to the centripetal force formula, the turning radius can be calculated as

$$r = \frac{m V^2}{L}, \tag{16}$$

where m is the mass of the Tunabot. Therefore, based on equations (10) and (14), we have

$$r \propto \frac{mA}{\rho LiSc} \left(\frac{f_1^2 (f_1 - \Delta f) + (f_1 - \Delta f)^2 f_1}{f_1^2 (f_1 - \Delta f) - (f_1 - \Delta f)^2 f_1} \right). \tag{17}$$

Since the mass, amplitude, fluid density, Lighthill number, the planform area and chord length of the

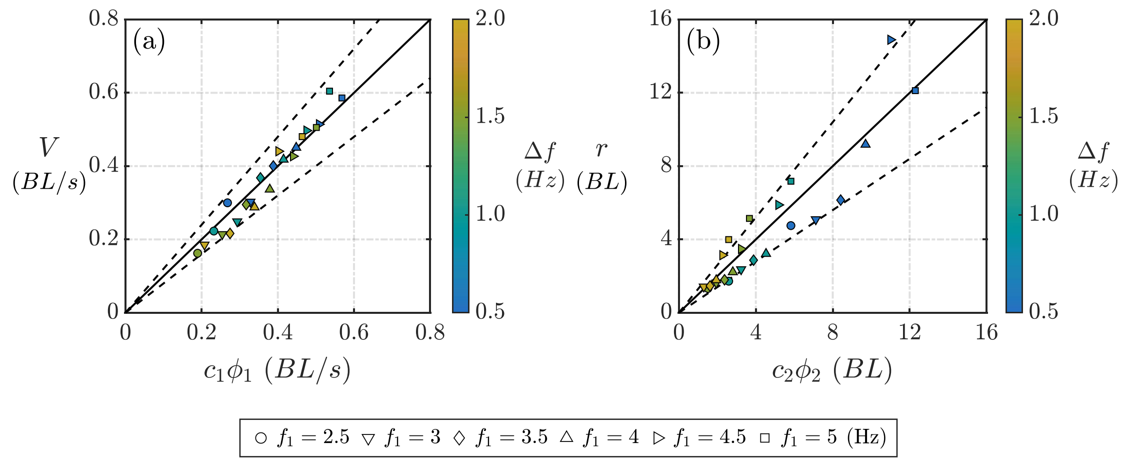

Figure 7. (a) Velocity and (b) turning radius compared with the scaling law predictions. Dashed lines present 20% and 30% margins of error in (a) and (b), respectively. If the scaling laws provide an accurate prediction of the velocity and turning radii, the data points should collapse to the line of $y = x$.

propulsor were fixed in our experiments, we can wrap them into a constant and have

$$r = c_2 \left(\frac{f_1^2 (f_1 - \Delta f) + (f_1 - \Delta f)^2 f_1}{f_1^2 (f_1 - \Delta f) - (f_1 - \Delta f)^2 f_1} \right), \tag{18}$$

where c_2 is a dimensional constant and needs to be determined. This constant is determined to be $c_2 = 0.65$ by linear regression. Figure 7(b) presents the scaling law prediction for the turning radius. The scaling law can predict the turning radius to within 30% error.

Furthermore, a scaling law for vehicle turning rate $\omega = V/r$ can be derived using equations (15) and (18) resulting in

$$\omega = c_3 \frac{\dfrac{f_1^2 (f_1 - \Delta f) - (f_1 - \Delta f)^2 f_1}{f_1^2 (f_1 - \Delta f) + (f_1 - \Delta f)^2 f_1}}{\sqrt{\dfrac{f_1^2 (f_1 - \Delta f) + (f_1 - \Delta f)^2 f_1}{2 f_1 - \Delta f}}} \tag{19}$$

where the coefficient is determined to be $c_3 = 0.17$ from c_1/c_2. With equation (19), parameter combinations of f_1 and Δf were optimized to determine the maximum turning rate of the vehicle. The optimization was performed using fmincon function in MATLAB over the parameter ranges of the experiments, which are $f_1 \in [2.5, 5.0]$ and $\Delta f \in [0.5, 2.0]$. The optimization presents that a combination of $f_1 = 5$ Hz and $\Delta f = 2$ Hz generates the maximum turning rate of $\omega = 9.60$ deg s^{-1}. The turning rate of this combination measured in experiments is $\omega = 7.03$ deg s^{-1}, exhibiting an error of 26.8%.

6. Turning power consumption

Figure 8 presents the power consumption of the data points in figure 6(a) and compares them with the power consumption of straight swimming. When the turning radius is fixed, the power is increased as the velocity is increased. In addition, at the same velocity, it requires more power to turn at a smaller turning radius. At low velocities ($V \leq 0.3$ BL s^{-1}), the power is increased by 7.8% to 36.8% compared to the straight swimming counterpart when the turning radius is $r = 1.6$ BL. At high velocities ($V > 0.3$ BL s^{-1}), a turning radius in the range $r = 3.2$ BL leads to a power increase ranging from 18.3% to 50.8% compared to the straight swimming. At low velocities, the power increase generated by turning can be negligible when the turning radius is large. For example, at the velocity of $V = 0.3$ BL s^{-1}, the power increase required to turn at a radius of $r = 4.75$ BL is only 2.61%.

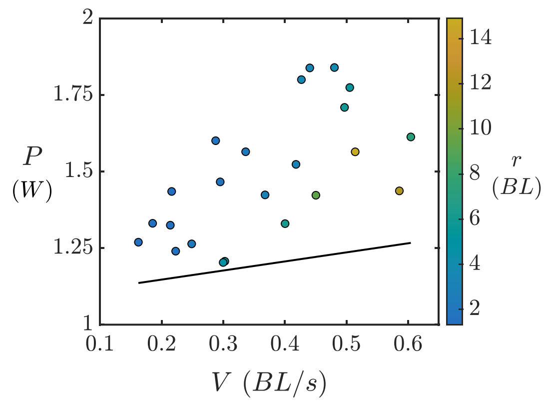

Figure 8. Power consumption as a function of the velocity. The black line represents the data for straight swimming, whose Δf is zero. The colored dots represent the data from asymmetric flapping. The marker color from blue to yellow represents increasing the turning radius.

7. Conclusions

This study demonstrates that targeted mechanical and control-based modifications to a tuna-like robot can successfully introduce turning capabilities without adding mechanical complexity to the vehicle. The selected control strategy successfully introduces a frequency asymmetry across the tailbeat cycle. Leveraging this frequency-based asymmetric flapping, the vehicle exhibits consistent and controllable turning maneuvers. Additionally, the turning radius and velocity of the Tunabot depend on the two input frequencies.

Lower base frequencies combined with a larger frequency difference leads to a turning maneuver with a smaller radius and reduced forward velocity, while higher base frequencies with smaller disparities led to a turning maneuver with faster swimming but a significantly larger radius.

Scaling laws were developed to reveal the physics behind the turning achieved by asymmetric flapping and can predict the velocity and turning radius of the Tunabot. It is discovered that the thrust and centripetal force acting on the Tunabot are dominated by the added mass force. The velocity scales with the square root of the added mass thrust, and the turning radius scales with the kinetic energy of the Tunabot over its added mass lift. Optimization of a scaling law to predict the turning rate of the vehicle reveals that the highest turning rate in the experimental range lies at the combination $f_1 = 5$ Hz, $\Delta f = 2$ Hz. Future work to further explore these hydrodynamic effects could include more comprehensive analysis, such as modeling of unsteady vortex dynamics and added mass effects through numerical simulation.

Executing a turning maneuver through the asymmetric flapping generates a power increase compared to the straight swimming at the same velocity. At low velocities ($V \leq 0.3$ BL s^{-1}), turning at a radius of $r \approx 1.6$ BL leads to 7.8% to 36.8% power increase compared to the straight swimming counterpart. At high velocities ($V > 0.3$ BL s^{-1}), a turning radius of $r \approx 3.2$ BL generates 18.3% to 50.8% increase in power compared to straight swimming. However, turning at low velocities with a large turning radius, for example $V = 0.3$ BL s^{-1} and $r = 4.75$ BL, generates negligible power increase.

This study presents a novel approach for the turning of underwater bio-robot achieved by frequency asymmetry across the tailbeat cycle. Moreover, this study quantifies the coupling among the velocity, turning radius, and power consumption during the turning maneuvers. These findings can help the design of highly maneuverable underwater bio-robots with low power consumption.

Data availability statement

All data that support the findings of this study are included within the article (and any supplementary files).

Acknowledgment

This work was supported by the Office of Naval Research under Program Director Dr Robert Brizzolara on MURI Grant No. N00014-22-1-2616.

ORCID iDs

Owen McKenney 0009-0003-5218-5473
Joseph Zhu 0000-0001-9941-6986
Tianjun Han 0000-0002-5319-123X
Hilary Bart-Smith 0000-0001-7469-7734

References

[1] Zhu J, White C, Wainwright D K, Di Santo V, Lauder G V and Bart-Smith H 2019 Tuna robotics: high-performance swimming for a soft-bodied fish robot *Sci. Robot.* **4** eaax4615

[2] White C H, Lauder G V and Bart-Smith H 2021 Tunabot Flex: a tuna-inspired robot with body flexibility improves high-performance swimming *Bioinspir. Biomim.* **16** 026019

[3] Hirata K, Takimoto T and Tamura K 2000 Study on turning performance of a fish robot *1st Int. Symp. On Aqua Bio-Mechanisms (ISABM)* pp 287–92

[4] Su Z, Yu J, Tan M and Zhang J 2013 Implementing flexible and fast turning maneuvers of a multijoint robotic *Fish IEEE/ASME Trans. Mechatronics* **19** 329–38

[5] Yu J, Wang M, Wang W, Tan M and Zhang J 2011 Design and control of a fish-inspired multimodal swimming robot *Proc. IEEE Int. Conf. Robot. Autom. (ICRA)* (https://doi.org/10.1109/ICRA.2011.5979652)

[6] Sitorus P E, Nazaruddin Y Y, Leksono E and Budiyono A 2009 Design and implementation of paired pectoral fins locomotion of labriform fish applied to a fish robot *J. Bionic Eng.* **6** 37–45

[7] Kato N 2000 Control performance in the horizontal plane of a fish robot with mechanical pectoral fins *IEEE J. Ocean. Eng.* **23** 121–29

[8] Li Z, Ge L, Xu W and Du Y 2018 Turning characteristics of biomimetic robotic fish driven by two degrees of freedom of pectoral fins and flexible body/caudal fin *J. Adv. Robot. Syst.* **15** 1729–8814

[9] Downs A M, Kolpas A, Block B A and Fish F E 2023 Multiple behaviours for turning performance of Pacific bluefin Tuna (Thunnus orientalis) *J. Exp. Biol.* **226** jeb244144

[10] Nath T, Mathis A, Chen A C, Patel A, Bethge M and Mathis M W 2019 Using DeepLabCut for markerless pose estimation across species and behaviors *Nat. Protocols* **14** 2152–76

[11] Theodorsen T 1979 General theory of aerodynamic instability and the mechanism of flutter *NACA Rep. 496*

[12] Han T, Zhong Q, Mivehchi A, Quinn D B and Moored K W 2024 Revealing the mechanism and scaling laws behind equilibrium altitudes of near-ground pitching hydrofoils *J. Fluid Mech.* **978** A5

[13] Moored K W and Quinn D B 2017 Inviscid scaling laws of a self-propelled pitching airfoil *AIAA J.* **57** 3686–700

[14] Theodorsen T and Garrick I E 1940 Mechanism of flutter: a theoretical and experimental investigation of the flutter problem *NACA Rep. 685*

[15] Eloy C 2013 On the best design for undulatory swimming *J. Fluid Mech.* **717** 48–89

[16] Akoz E and Moored K W 2018 Unsteady propulsion by an intermittent swimming gait *J. Fluid Mech.* **834** 149–72